

L-EGCG-Mn nanoparticles as a pH-sensitive MRI contrast agent

Jiali Li^{a,*}, Xue Jiang^{b,c,*}, Lihuan Shang^c, Zhen Li^a, Conglian Yang^c, Yan Luo^a, Daoyu Hu^a, Yaqi Shen^a and Zhiping Zhang^{c,d,e}

^aDepartment of Radiology, Tongji Hospital, Tongji Medical College, Huazhong University of Science and Technology, Wuhan, China;

^bGuangdong Provincial Key Laboratory of Malignant Tumor Epigenetics and Gene Regulation, Medical Research Center, Sun Yat-sen Memorial Hospital, Sun Yat-sen University, Guangzhou, China; ^cTongji School of Pharmacy, Huazhong University of Science and Technology, Wuhan, PR China; ^dNational Engineering Research Center for Nanomedicine, Huazhong University of Science and Technology, Wuhan, PR China; ^eHubei Engineering Research Center for Novel Drug Delivery System, Huazhong University of Science and Technology, Wuhan, PR China

ABSTRACT

This study aimed to synthesize and characterize L-epigallocatechin gallate (EGCG) complexed Mn²⁺ nanoparticle (L-EGCG-Mn), a proof-of-concept pH-sensitive manganese core nanoparticle (NP), and compare its magnetic resonance (MR) properties with those of Gd-DTPA, both *in vitro* and *in vivo*. Reverse microemulsion was used to obtain the L-EGCG-Mn NPs. The physicochemical properties of L-EGCG-Mn were characterized using dynamic light scattering, transmission electron microscopy, and near-infrared fluorescence small animal live imaging. The *in vitro* relaxivity of L-EGCG-Mn incubated with different pH buffer solutions (pH = 7.4, 6.8, 5.5) was evaluated. The T1-weighted MR imaging (MRI) properties were evaluated *in vitro* using hypoxic H22 cells as well as in H22 tumor-bearing mice. Cytotoxicity tests and histological analysis were performed to evaluate the safety of L-EGCG-Mn. L-EGCG-Mn showed good biocompatibility, stability, pH sensitivity, and tumor-targeting ability. Moreover, when the pH was decreased from 7.4 to 5.5, the r_1 relaxivity of L-EGCG-Mn was shown to gradually increase from 1.79 to 6.43 mM⁻¹·s⁻¹. Furthermore, after incubation with L-EGCG-Mn for 4 h, the T1 relaxation time of hypoxic H22 cells was significantly lower than that of normoxic H22 cells (1788 ± 89 vs. 1982 ± 68 ms, $p = .041$). The *in vivo* analysis showed that after injection, L-EGCG-Mn exhibited a higher MRI signal compared to Gd-DTPA in H22 tumor-bearing mice ($p < .05$). Furthermore, L-EGCG-Mn was found to have a good safety profile via cytotoxicity tests and histological analysis. L-EGCG-Mn has a good safety profile and pH sensitivity and may thus serve as a potential MRI contrast agent.

ARTICLE HISTORY

Received 22 October 2020
Revised 4 December 2020
Accepted 7 December 2020

KEYWORDS

MRI contrast agent;
nanoparticle; manganese;
EGCG; pH sensitivity


Introduction

Cancer cells rely on the 'Warburg effect' for aerobic glycolysis, leading to the accumulation of high lactate concentrations, even under aerobic conditions (Peng et al., 2019). Although the presence of lactate in the tumor microenvironment (TME) was previously considered as metabolic waste, more recently, accumulating evidence has suggested that it acts as an important signaling molecule in the regulation of tumor metabolism and immunity (Zhang et al., 2019). Moreover, the lactate in the TME controls multiple phenomena associated with tumor resistance to therapy (Pilon-Thomas et al., 2016; Ippolito et al., 2019). Thus, the noninvasive detection of tumor acidic regions is critical not only for personalized medicine but also for prognosis prediction. The physiological pH of normal tissues and body fluids (including blood) is approximately neutral (7.35–7.45), whereas the pH

of tumor tissues is more acidic (6.5–7.0), which decreases even further in hypoxic regions *in vivo* (<6.5) (Neri & Supuran, 2011). Engineered nanoparticles (NPs) that respond to acidic pH (<6.5) and release paramagnetic components are expected to reflect tumor lactate level via magnetic resonance imaging (MRI) (Garcia-Hevia et al., 2019).

The earliest and most frequently used MRI contrast agent (CA) approved for clinical use was Gd³⁺-complexes. However, the safety of Gd-DTPA-BMA (gadodiamide) has become increasingly controversial since 2006 (Grobner, 2006; Marckmann et al., 2006). Currently, in addition to two hepatocyte-specific CAs, European countries ban the use of Gd-BOPTA (gadobenate dimeglumine), Gd-DTPA-BMA, Gd-DTPA (gadopentetate dimeglumine), and Gd-DTPA-BMEA (gadoversetamide) (Dekkers et al., 2018). Mn, an essential trace element in the human body, was shown to have a short T1 effect

CONTACT Yaqi Shen  yqshen@hust.edu.cn  Department of Radiology, Tongji Hospital, Tongji Medical College, Huazhong University of Science and Technology, Wuhan, China; Zhiping Zhang  zhipingzhang@mail.hust.edu.cn  Tongji School of Pharmacy, Huazhong University of Science and Technology, Wuhan, PR China

 Supplemental data for this article can be accessed [here](#).

*These authors contributed equally to this work.

© 2020 The Author(s). Published by Informa UK Limited, trading as Taylor & Francis Group.

This is an Open Access article distributed under the terms of the Creative Commons Attribution License (<http://creativecommons.org/licenses/by/4.0/>), which permits unrestricted use, distribution, and reproduction in any medium, provided the original work is properly cited.

due to its five unpaired electrons (Reddi et al., 2009; Pan et al., 2011). Hence, Mn^{2+} -based CAs have become of high interest for the development of novel MRI CAs (Gale et al., 2015; Erstad et al., 2019). In the last decade, scientists have developed numerous Mn-based NPs for tumor-specific MRI. Nevertheless, in the case of some CAs (Shin et al., 2009; Huang et al., 2010a, 2010b), the Mn^{2+} was trapped/coordinated in the NP, resulting in lower relaxation efficiency compared to free Mn^{2+} . Recently, intelligent NPs (Cai et al., 2015; Mi et al., 2016; Li et al., 2017; Wang et al., 2018), which respond to the acidic conditions in tumor tissues, have been designed to improve the accuracy and sensitivity of imaging techniques by increasing the contrast between the tumor tissue and background. For example, one strategy involves Mn^{2+} doping into calcium phosphate (CaP) (Mi et al., 2016) or silica (Kim et al., 2013) to form pH-sensitive CAs. However, the inevitable degradation problem of these inorganic agents appears to limit further clinical applications (Fu et al., 2019). In contrast, epigallocatechin gallate (EGCG), an organic green tea extract with excellent antioxidant activity, has gained increasing attention in the biomedical field due to its good biocompatibility, pH sensitivity, and versatile functionalization capabilities (Reygaert, 2014, 2018). For example, NPs coordinating EGCG with metal ions, such as Fe^{3+} (Xiao et al., 2015), Cu^{2+} (Tsai et al., 2016), Au^{3+} (Jiang et al., 2019), or Sm^{3+} (Li et al., 2019), have been used to diagnose and treat tumors and have had impressive safety assessments. However, there are few studies on the chelation of EGCG with Mn^{2+} for MRI.

As such, in this study, we fabricate a novel NP based on the chelation effect of EGCG and Mn^{2+} and obtained NPs that might be used as an MRI CA (Figure 1). The coordination interaction between the metal and EGCG was evaluated by previous studies (Rahim et al., 2018; Wang et al., 2018). Moreover, PEGylation was shown to enhance the stability of L-epigallocatechin gallate (EGCG) complexed Mn^{2+} nanoparticle (L-EGCG-Mn) and prolong circulation time (Li et al., 2010; Calcagno et al., 2019). In addition, the chelation of EGCG to Mn^{2+} would be weakened in an acidic environment (Navarro et al., 2005), thereby accelerating the release of Mn^{2+} . Thus, L-EGCG-Mn could be disintegrated in a low pH environment to accurately control Mn^{2+} release and simultaneously present high relaxivity.

This study aimed to synthesize and characterize the pH-sensitive L-EGCG-Mn as well as verify its magnetic resonance (MR) properties, both *in vitro* and *in vivo*. The first commercially approved Gd chelate, Gd-DTPA, was used as the reference standard for MRI CA.

Materials and methods

This study was approved by the local Ethics Committee and all experiments in this study strictly followed the Institutional Guidelines of Experimental Animal Care and Use. The entire workflow of this study is briefly shown in Figure 2.

Materials

Manganese chloride ($MnCl_2$), cyclohexane, and cobalt (iii) chloride hexahydrate ($CoCl_2$) were purchased from Aladdin[®] (Shanghai, China). EGCG was obtained from Purify[®] (Chengdu, China) and IGEPAL CO-520 was obtained from Sigma-Aldrich (St. Louis, MO). Dioleoyl phosphatidic acid (DOPA), 1,2-dioleoyl-snglycero-3-phosphocholine (DOPC), cholesterol, and 1,2-dioleoyl-sn-glycero-3-phosphoethanol-amine-N-[methoxy(polyethylene, glycol)-2000] (DSPE-PEG2000) were purchased from Avanti Polar Lipids, Inc. (Alabaster, AL), whereas 1,1'-dioctadecyl-3,3',3'-tetramethylindotricarbocyanine iodide (DiR) was purchased from AAT Bioquest, Inc. (Sunnyvale, CA). The 3-(4, 5-dimethyl-thiazol-2-yl)-2,5-diphenyltetrazolium bromide (MTT) was obtained from BioSharp (Seoul, South Korea).

Preparation of L-EGCG-Mn NPs

EGCG-Mn/DOPA NPs (EGCG-Mn NPs) were prepared using the reverse microemulsion method (Zhuang et al., 2016). Phase A, consisting of 100 μ L of 10 mM EGCG and 100 μ L of DOPA, was added to 4 mL CO-520/cyclohexane, and phase B, consisting of 100 μ L of 80 mM $MnCl_2$ was added to 4 mL CO-520/cyclohexane, and stirred separately for 0.5 h to form a reverse water-in-oil microemulsion. Next, phase A was added dropwise to phase B while stirring. After 2 h, 8 mL of ethyl alcohol was added to break the microemulsion. The mixture was then collected and centrifuged at 13,000 \times g for 15 min. Thereafter, the precipitate was washed twice with ethyl alcohol and dried using N_2 .

The L-EGCG-Mn NPs were prepared by dissolving EGCG-Mn/DOPA, 80 μ L of 20 mM DOPC, 80 μ L of 20 mM cholesterol, and 20 μ L of 20 mM DSPE-PEG2000 in 4 mL trichloromethane. Next, trichloromethane was removed via rotary evaporation. DiR-labeled L-EGCG-Mn was prepared by dissolving EGCG-Mn/DOPA, DiR, DOPC, cholesterol, and DSPE-PEG2000 in trichloromethane, and the trichloromethane was removed with rotary evaporation. The L-EGCG-Mn NPs or DiR-labeled L-EGCG-Mn were then hydrated using phosphate-buffered saline (PBS) and incubated in a water bath at 37 °C for 0.5 h and then used for further applications.

Characterization of the L-EGCG-Mn NPs

Zeta potential and particle size were measured via dynamic light scattering (DLS, ZetaPlus, Brookhaven Instruments, Holtsville, NY). Their morphology was evaluated through transmission electron microscopy (TEM, HITACHI H-7000 FA, Chiyoda City, Japan, acceleration voltage = 100 kV). The stability of the L-EGCG-Mn NPs was investigated by dispersing the L-EGCG-Mn NPs in PBS and fetal bovine serum (FBS). Thereafter, the change in particle size was recorded continuously for 1 week.

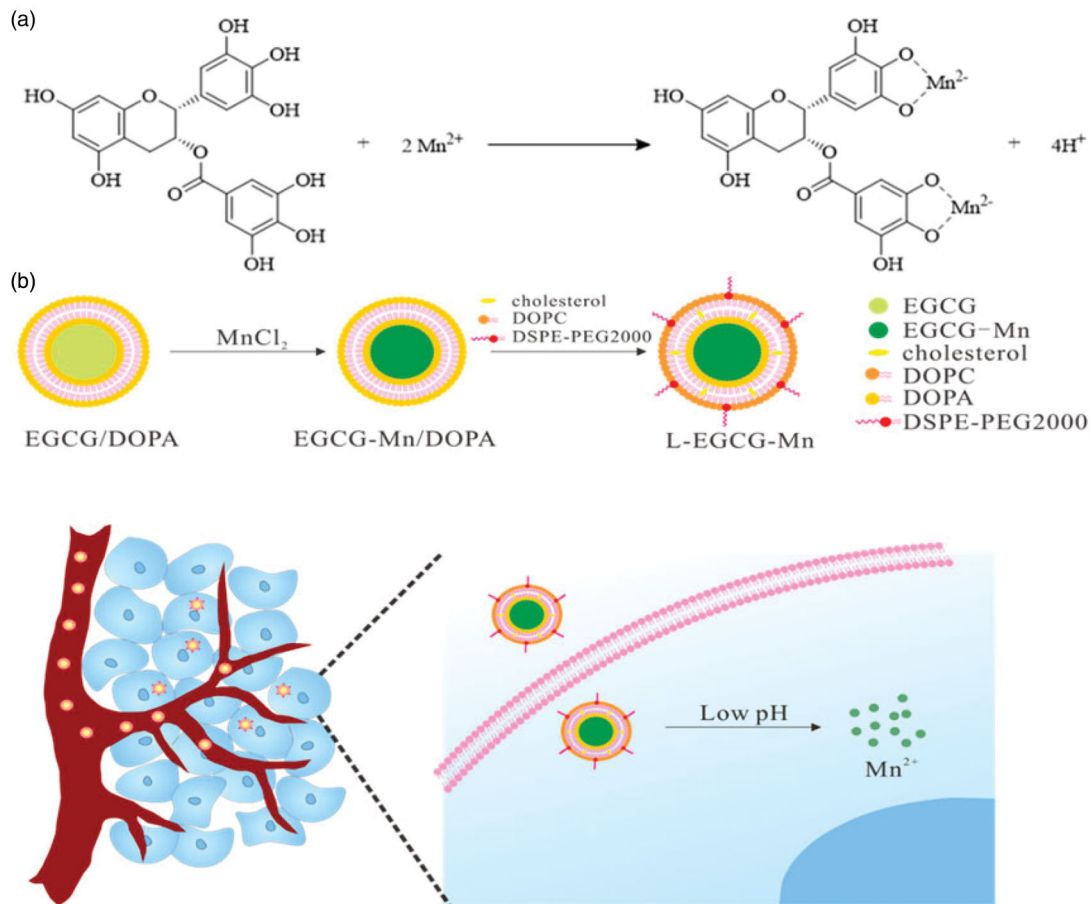
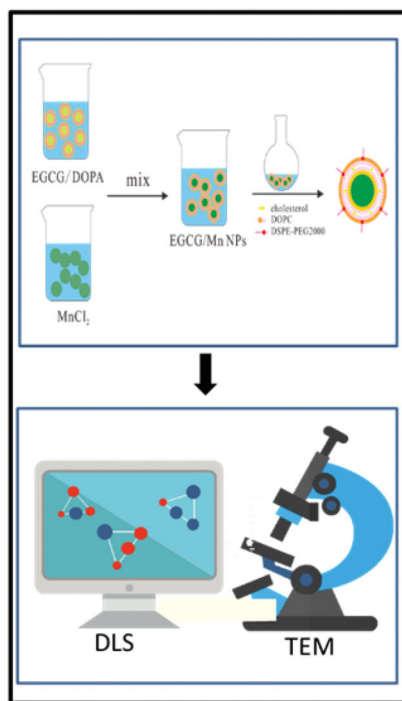
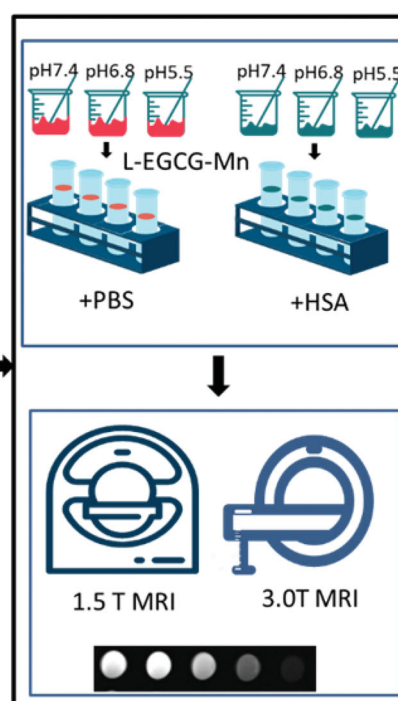


Figure 1. A scheme indicating the synthesis of L-EGCG-Mn NPs and the subsequent pH-sensitive mechanism *in vivo*. (a) Mn^{2+} coordinated with EGCG to form EGCG-Mn complexes. (b) The preparation of L-EGCG-Mn NPs and the mechanism of action of L-EGCG-Mn NPs *in vivo*.

Step 1: synthesis and characterization



Step 2: relaxivity measurement



Step 3: *in vivo* MRI assessment

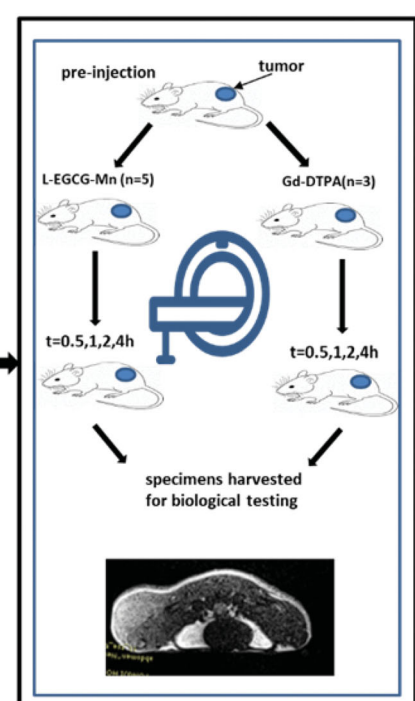


Figure 2. Flowchart of the entire experimental design. Step 1, synthesis and characterization. The reverse microemulsion method was used to obtain L-EGCG-Mn NPs. Step 2, relaxivity measurement. In each set of L-EGCG-Mn solution, the Mn concentration used was 0.04, 0.08, 0.2, 0.4, and 0.8 mM, respectively. Three samples per concentration were analyzed. Step 3, *in vivo* MRI assessment. Eight mice who received H22 cell transplantation were imaged using a 3 T MRI scanner ($n = 5$ injected with L-EGCG-Mn NPs, $6.4 \mu\text{mol/kg Mn}$; $n = 3$ injected with Gd-DTPA, $6.4 \mu\text{mol/kg Gd}$).

Cell lines and tumor model

H22 and L929 cells were purchased from the Chinese Academy of Sciences Cells Bank (Shanghai, China). Cells were maintained in Dulbecco's Modified Eagle Medium (L929) or Roswell Park Memorial Institute-1640 medium (H22) supplemented with 10% FBS and 1% penicillin and streptomycin under a humidified atmosphere (37 °C, 5% CO₂). KM mice (female, 18–20 g; 4–5 weeks of age) were purchased from the local institutional animal care center and were acclimated to the center environment before study initiation.

After resuscitation, H22 cells were injected into the peritoneal cavity of KM mice. Carcinoma ascites were collected after seven days. The concentration of H22 cells was adjusted to 2×10^6 cells/mL, and 100 μ L of the H22 cell suspension was subcutaneously injected into the left side of the mice back to generate the tumor model (Bao et al., 2016).

In vitro cytotoxicity evaluation

Cytotoxicity was evaluated using the MTT assay. Briefly, normal fibroblasts cells L929 were seeded in 96-well plates at a density of 8000 cells/well and cultured for 24 h. Next, the supernatant was removed and replaced with 100 μ L of blank medium supplemented with various concentrations of L-EGCG-Mn NPs. After incubating for another 24 h, 10 μ L of MTT (5 mg/mL) was added and the cells were then incubated for another 2 h. The liquid from each well was removed and replaced with 150 μ L of dimethyl sulfoxide. The absorbance at 490 nm was detected using a microplate reader (Multiskan MK3, Thermo Fisher Scientific, Waltham, MA).

Relaxivity measurement

Preparation of samples

Three sets of L-EGCG-Mn buffer solutions with different pH values (pH = 7.4, 6.8, and 5.5 PBS) were prepared. The Gd-DTPA in PBS (pH = 7.4) solution was used as a control. For each set of the L-EGCG-Mn solutions, the Mn concentrations used were 0.04, 0.08, 0.2, 0.4, and 0.8 mM. Likewise, the Gd concentration in the Gd-DTPA solution was 0.04, 0.08, 0.2, 0.4, and 0.8 mM. Three samples per concentration were analyzed. Thus, this group contained a total of 60 samples.

Forty-five more samples were prepared in the same manner and incubated with human serum albumin (HSA, 10 mg/mL) for 24 h. Fresh samples were prepared before the MR scan. Finally, 210 samples were analyzed via MR scanning (1.5 and 3 T at 22 °C).

After MR scanning, the final Mn concentration of the L-EGCG-Mn buffer solutions (180 samples) was measured via flame atomic absorption spectroscopy (SpectrAA-240FS, Varian, Palo Alto, CA) (wide range [Mn²⁺], 0.02–0.6 mM). Nitric acid was added to decompose the L-EGCG-Mn NPs before detection.

Machine and sequences

In vitro analysis was performed on a 1.5 T (Aera; Siemens, Healthcare, Erlangen, Germany) MR scanner with a Tx/Rx

15-channel knee coil and a 3 T (Skyra; Siemens Healthcare, Erlangen, Germany) MR system with a Tx/Rx 15-channel knee coil. T₁ maps were obtained using a series of inversion-recovery sequences with various inversion times (TIs) (Ogg & Kingsley, 2004; Shen et al., 2015). TI = [30, 60, 90, 120, 150, 250, 400, 600, 800, 1200, 1600, 2000, 2400, 2800, and 3200] ms. The repetition time (TR) was equal to 1500 ms + TI. The echo time (TE) was 15 (3 T)/11 (1.5 T) ms. The T₂ maps were obtained using a protocol involving multi-echo spin-echo sequences (Pintaske et al., 2006; Shen et al., 2019): the TE was between 20 and 600 ms with an interval of 20 ms and the TR was 3000 ms. The following parameters were maintained for all measurements: slice thickness, 5 mm; field-of-view, 80 × 100 mm; matrix, 256 × 256.

Calculation of relaxivity

First, the generated DICOM images were analyzed via the ImageJ software package (open source, National Institutes of Health, Bethesda, MD), which was used to place fixed-size circular region-of-interest (ROI) and to automatically calculate mean signal intensities (SIs) within the ROI. ROIs were between 160 and 170 pixels. Second, the relaxivity constants R_1 and R_2 are determined via Equations (1) and (2), respectively, using a developed Data fitting software (Sigma Plot 12.5).

$$SI_{T1} = A_1 + B_1 \exp^{-R_1 \cdot TI} \quad (1)$$

$$SI_{TE} = A_2 \exp^{-R_2 \cdot TE} + B_2 \quad (2)$$

Finally, the r_1 and r_2 values are obtained using Equation (3) (Fries et al., 2015). Here, $R(c)$ denotes the relaxivity constant of L-EGCG-Mn at concentration C and $R(0)$ represents the relaxivity constant of PBS or HSA.

$$r = (R(c) - R(0)) / C \quad (3)$$

Cellular MR imaging

To evaluate the MR properties of L-EGCG-MN NPs in normoxic and hypoxic cells, CoCl₂ was used to induce chemical hypoxia (Dubbelboer et al., 2019). Briefly, H22 cells were isolated under sterile conditions and were randomly assigned to either the hypoxia and normoxia groups. Cells were then incubated with medium with or without CoCl₂ (200 μ M) and seeded into six-well plates (1×10^7 cells/well) for 12 h. The cells were then collected and the medium was removed via centrifugation. Thereafter, the cells were washed thrice with PBS to eliminate the residual CoCl₂. The cells were then resuspended in medium with or without L-EGCG-Mn (1 mM). After being incubated for 4 h, the cells were washed thrice with PBS to eliminate the residual L-EGCG-Mn. Next, agarose gel (1%, 300 μ L) was used to resuspend and fix the cells (Zheng et al., 2019). Finally, cellular imaging was carried out using the abovementioned MR system (3 T).

Animal MRI

H22 tumor-bearing mice were used for animal MRI assessments. Tumor growth occurred in 10 days and the final tumor volume was approximately 100 mm^3 . The tumor volume was measured from vernier caliper and calculated as the length \times width (Zhang et al., 2019) $\times 0.5$ (Luo et al., 2019). All mice were scanned using a 3.0 T MRI scanner (Skyra; Siemens Healthcare, Erlangen, Germany) with an 8-channel 5-cm Rx custom-design coil. Anesthetized animals were kept warm with a thermostatic electric blanket at 37°C between imaging sessions. Before imaging, the animals were placed in a prone position. T1 images were acquired pre-injection and at 0.5, 1, 2, and 4 h after the injection of L-EGCG-Mn ($6.4\ \mu\text{mol/kg}$ Mn) and Gd-DTPA ($6.4\ \mu\text{mol/kg}$ Gd) NPs via the tail vein. The time points were selected based on a previously published study by Mi et al. (2016). The detailed scanning parameters are listed in [supplementary Table 1](#).

Image analysis: signal-to-noise ratio (SNR) and contrast-to-noise ratio (CNR) were measured and calculated by two radiologists based on previous reports (Peng et al., 2018), using Equations (4) and (5), respectively:

$$\text{SNR} = S_{\text{tumor}} / SD_{\text{background}} \quad (4)$$

$$\text{CNR} = |S_{\text{tumor}} - S_{\text{tissue}}| / \sqrt{SD_{\text{tumor}}^2 + SD_{\text{tissue}}^2} \quad (5)$$

where S_{tumor} represents the SI in the ROI placed on a homogeneously enhancing part of the tumor without necrosis and $SD_{\text{background}}$ represents the standard deviation of the background noise. S_{tissue} represents the SI in the ROI of ipsilateral normal muscle tissue. SD_{tumor} and SD_{tissue} represent the standard deviation of the tumor and normal tissue. The ROIs were located in anatomic positions, which were as accurate as possible for the different time points. The above parameters were measured by two experienced radiologists blinded to the CA administered. The average was then obtained for further analysis.

Fluorescence imaging and in vivo distribution of L-EGCG-Mn

DiR (ex = 748 nm, em = 780 nm) can be used to obtain the vivo fluorescence images. Thus, the L-EGCG-Mn NPs were labeled with DiR to investigate their distribution. DiR-labeled L-EGCG-Mn ($200\ \mu\text{L}$, approximately $4\ \mu\text{g}$ DiR per mouse) were injected intravenously. Mice injected with DiR dissolved in PBS were used as a negative control. The mice were euthanized and the heart, liver, spleen, lung, kidneys, tumor, and homolateral inguinal lymph nodes were excised and photographed using a near-infrared fluorescence small animal live imaging system (Pearl Trilogy, LI-COR) at 1, 2, 4, 8, 12, and 24 h post-injection.

Histological analysis

All mice were euthanized after the last MRI analysis. Afterwards, the specimens, including the major organs (heart, liver, spleen, lung, kidneys), tumor, and homolateral inguinal lymph nodes, were harvested and fixed via immersion in

10% formalin. After paraffin embedding and hematoxylin and eosin staining, the sample sections were evaluated by an experienced histopathologist.

Statistical methods

All statistical analyses were completed using IBM SPSS 23.0 (Chicago, IL) and GraphPad Prism 7.0 (GraphPad Software, La Jolla, CA). A p value $< .05$ was considered to be statistically significant. The measurement consistency between the two radiologists was tested by calculating the interclass correlation coefficient (ICC). Continuous variables were analyzed using the Kolmogorov–Smirnov test to determine the normality and then, the Student t -test (normal distribution) or Mann–Whitney U -test (non-normal distribution) was used for comparison.

Results

Characterization of L-EGCG-Mn NPs

The particle size of the L-EGCG-Mn NPs was $277.4 \pm 5.5\ \text{nm}$ (Figure 3(a)) and the zeta potential was $-13.56 \pm 1.91\ \text{mV}$. Moreover, the particle size change after incubation in both PBS and FBS for 1 week was negligible (Figure 3(b), supplementary figure 1). DLS (Figure 3(c)) showed that the particle size of L-EGCG-Mn NPs incubated with an acidic solution increased over time, with L-EGCG-Mn NPs in a solution with a pH of 5.5 expanding faster than those in a solution with a pH of 6.8. The morphology determined via TEM (Figure 4) revealed that there was a change between L-EGCG-Mn NPs incubated in a solution with a pH of 7.4 or 5.5. In addition, we also observed that the NPs disintegrated in an acidic environment.

In vitro cytotoxicity evaluation

L929 cells were used to assess the cytotoxicity of L-EGCG-Mn NPs in normal cells. As shown in Figure 5, cell viability was not markedly reduced when L929 cells were incubated with L-EGCG-Mn NPs for 24 h.

Relaxivity measurement

The plots of signal vs. T1 or TE and of R1 or R2 vs. [Mn] are shown in [supplementary figure 2](#). The relaxivity values of L-EGCG-Mn and Gd-DTPA at 1.5 and 3.0 T are presented in [Table 1](#). For the 3 T MRI, when the pH decreased from 7.4 to 5.5, the r_1 (r_2) value of L-EGCG-Mn NPs increased from 1.79 (10.79) to 6.43 (41.78) $\text{mM}^{-1} \cdot \text{s}^{-1}$ in the buffer solution and from 1.77 (16.1) to 7.23 (42.56) $\text{mM}^{-1} \cdot \text{s}^{-1}$ in HSA. Moreover, there was a significant difference in the relaxivity values between the L-EGCG-Mn NP solutions with different pH ($p < .001$, Figure 6). At pH 5.5, the relaxivity values (r_1 and r_2) of L-EGCG-Mn NPs were found to be higher than that of Gd-DTPA ($p < .001$).

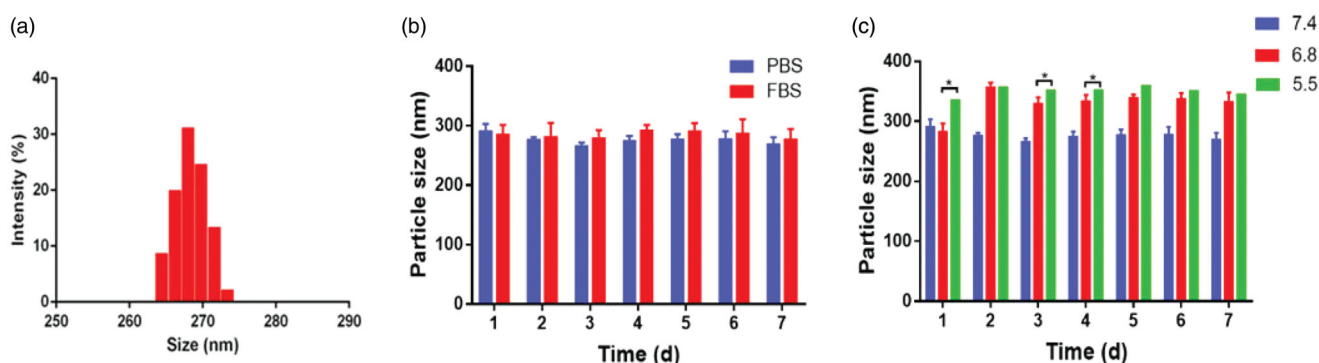


Figure 3. Characterization of L-EGCG-Mn NPs. (a) Particle size of L-EGCG-Mn NPs. (b) The change in particle size of L-EGCG-Mn NPs in phosphate-buffered saline (PBS) and fetal bovine serum (FBS) during a time period of seven days after preparing the solution. (c) The change in particle size of L-EGCG-Mn NPs incubated in buffer solutions with a pH of 7.4, 6.8, or 5.5.

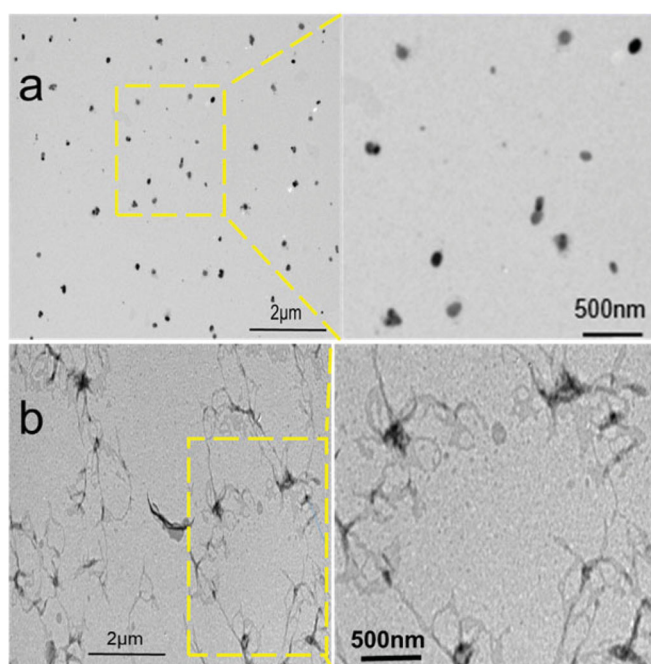


Figure 4. TEM images of L-EGCG-Mn NPs incubated with (a) pH 7.4 buffer solution and (b) pH 5.5 buffer solution.

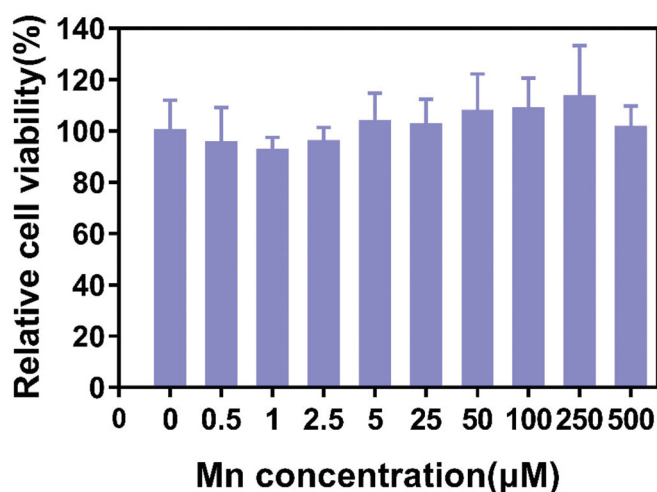


Figure 5. Evaluation of *in vitro* cytotoxicity of L-EGCG-Mn NPs in L929 cells.

Cellular MR imaging

The shortening of the T1 relaxation time (ΔT_1) was calculated by subtracting T1 value for a Mn concentration of 1 mM from the T1 value for 0 mM Mn. After incubation with L-EGCG-Mn NPs for 4 h, the T1 value of hypoxic H22 cells was found to be significantly lower than that of normoxic H22 cells (1788 ± 89 vs. 1982 ± 68 ms, $p = .041$) (Figure 7, supplementary Table 2). Moreover, the ΔT_1 of the hypoxia group was shown to be lower than that of the normoxia group (817 vs. 993 ms).

Animal MRI

The interobserver agreement for CNR and SNR was excellent ($ICC > 0.81$, Table 2). For L-EGCG-Mn and Gd-DTPA, the CNR and SNR almost reached their peak at 1 h, followed by a stable high value for the former but a downtrend for the latter (Figure 8). After injection, the average value of CNR and SNR was significantly higher for L-EGCG-Mn NPs than for Gd-DTPA at all acquired timepoints ($p < .05$, supplementary table 3). The classic MRI images of the two mice groups are shown in Figure 9.

Fluorescence imaging and *in vivo* distribution of L-EGCG-Mn NPs

The DiR-L-EGCG-Mn NPs were found to gradually gather at the tumor site after injection, with the quantity of NPs at the site increasing over time. Moreover, the fluorescence intensity at the tumor site in the DiR-L-EGCG-Mn group was evidently stronger than that in the DiR group (Figure 10). The fluorescence intensity in the inguinal lymph nodes was also stronger in the DiR-L-EGCG-Mn group than that of the DiR group.

Histological analysis

Histopathological analysis confirmed the presence of hepatoma cells in the tumor samples from all examined animals (supplementary figure 3). After L-EGCG-Mn injection, no appreciable abnormalities were observed in the heart, liver,

Table 1. *In vitro* MRI relaxivities of L-EGCG-Mn and Gd-DTPA.

Contrast agents	1.5 T		3 T	
	r_1 ($\text{mM}^{-1}\cdot\text{s}^{-1}$)	r_2 ($\text{mM}^{-1}\cdot\text{s}^{-1}$)	r_1 ($\text{mM}^{-1}\cdot\text{s}^{-1}$)	r_2 ($\text{mM}^{-1}\cdot\text{s}^{-1}$)
L-EGCG-Mn(+HSA)				
pH 7.4	1.23 ± 0.09 (2.08 ± 0.41)	8.06 ± 0.51 (10.13 ± 1.42)	1.79 ± 0.004 (1.77 ± 0.05)	10.79 ± 0.47 (16.10 ± 1.08)
pH 6.8	2.14 ± 0.37 (2.63 ± 0.71)	13.54 ± 2.09 (14.33 ± 2.48)	4.18 ± 0.04 (5.55 ± 0.06)	20.26 ± 0.38 (26.95 ± 0.37)
pH 5.5	5.93 ± 0.04 (6.45 ± 0.19)	37.59 ± 0.70 (38.09 ± 2.02)	6.43 ± 0.05 (7.23 ± 0.02)	41.78 ± 2.12 (42.56 ± 2.17)
Gd-DTPA	4.38 ± 0.001	4.9 ± 0.03	4.99 ± 0.09	5.99 ± 0.13

MRI: magnetic resonance imaging; Gd: gadolinium; HSA: human serum albumin. Values are given as mean ± SD in buffered saline (in HSA) at room temperature.

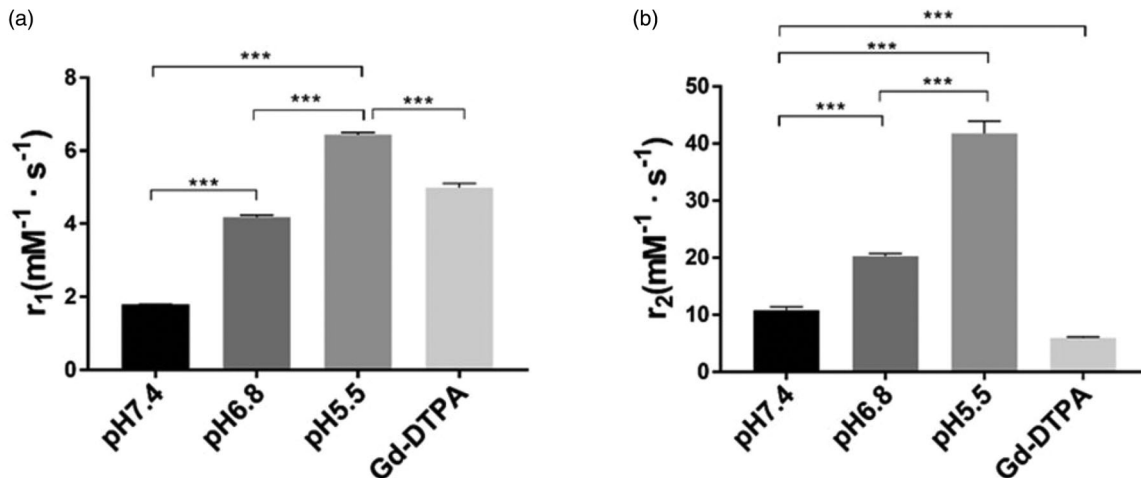


Figure 6. *In vitro* relaxivity. (a, b) The r_1 and r_2 relaxivity of L-EGCG-Mn NPs at different pH values and Gd-DTPA in 3 T MRI. pH 7.4 and 6.8 phosphate buffer solution and pH 5.5 acetate buffer solution were used here. Data are shown as mean ± SD. ($n = 3$), $***p < .001$.

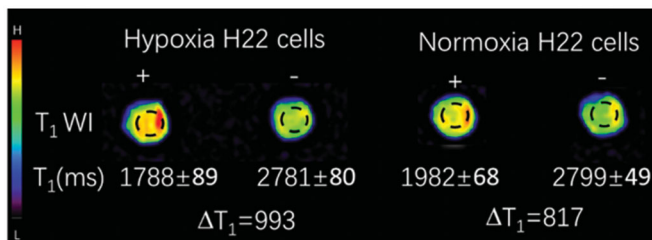


Figure 7. T1-weighted H22 cellular MRI with (+) and without (-) L-EGCG-Mn NPs. The T1 value was obtained from the T1 mapping images. ΔT_1 was calculated by subtracting the T1 value for 1 mM Mn from the T1 value for 0 mM Mn.

Table 2. The inter-observer agreement between two radiologists of CNR and SNR.

Parameters	ICC	95% CI
CNR	0.960	0.924–0.979
SNR	0.899	0.806–0.948

ICC: interclass correlation coefficient; CI: confidence interval.

spleen, lungs, and kidneys. Reactive hyperplasia was observed in the tumor homolateral inguinal lymph node.

Discussion

Contrast-enhanced MRI fulfills several important medical needs. Therefore, the development and improvement of MRI CAs, especially tumor-targeting agents, is a growing area of study (Adisheshaiah et al., 2013; Gale et al., 2018). The acidic pH environment, mainly caused by lactate, has been extensively proven to be a tumor-specific characteristic (Kanamala

et al., 2016). As such, this study aimed to synthesize pH-sensitive NPs to develop a tumor-targeting MRI CA.

We designed a series of experiments to demonstrate the pH-sensitivity of L-EGCG-Mn NPs. First, L-EGCG-Mn NPs were incubated with buffer solutions of a different pH. Analysis of the change in particle size and morphology implied that L-EGCG-Mn NPs were disrupted in low pH environments. Moreover, *in vitro* analysis indicated that the relaxivity of L-EGCG-Mn NPs increased as the pH decreased. The T1 value of L-EGCG-Mn NPs in hypoxic cells was also lower than that found in normoxic cells, which suggests that L-EGCG-Mn NPs are sensitive to pH at the cellular level. These findings supported our hypothesis that a low pH could mediate the disassembly of L-EGCG-Mn NPs and accurately control the release of Mn^{2+} (Li et al., 2010). Thus, we can reasonably assume that L-EGCG-Mn NPs may be applicable for tumor imaging, where the specific acidic environment can serve as relaxation switches activated by pH (Li et al., 2010). Our results also showed that L-EGCG-Mn NPs mainly released Mn^{2+} in the tumor area, which enabled the selective enhancement of tumor tissue and thus increased the contrast between tumor and adjacent normal tissues. In addition, pH-sensitive L-EGCG-Mn NPs may help predict and assess tumor therapeutic outcomes, as an acidic environment is greatly associated with therapeutic response (Swartz et al., 2012; Chang et al., 2015; Pilon-Thomas et al., 2016). However, this hypothesis requires further experimental verification.

Analysis of DiR-L-EGCG-Mn distribution *ex vivo* showed that L-EGCG-Mn NPs possessed excellent tumor-targeting abilities for approximately 24 h post-injection, which could

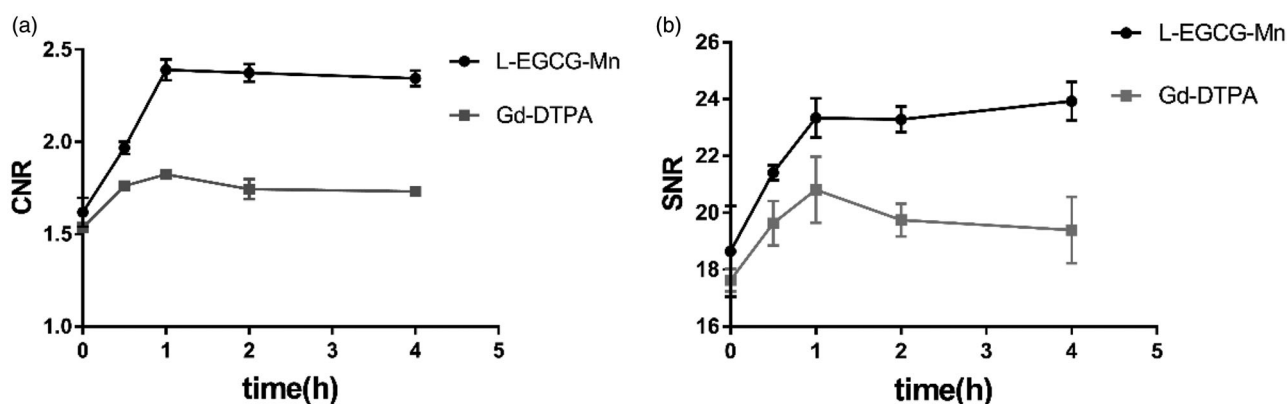


Figure 8. The contrast-to-noise ratio (CNR) and signal-to-noise ratio (SNR) evaluation. (a, b) The trend of CNR and SNR after the administration of L-EGCG-Mn ($n=5$) and Gd-DTPA ($n=3$) for T1WI.

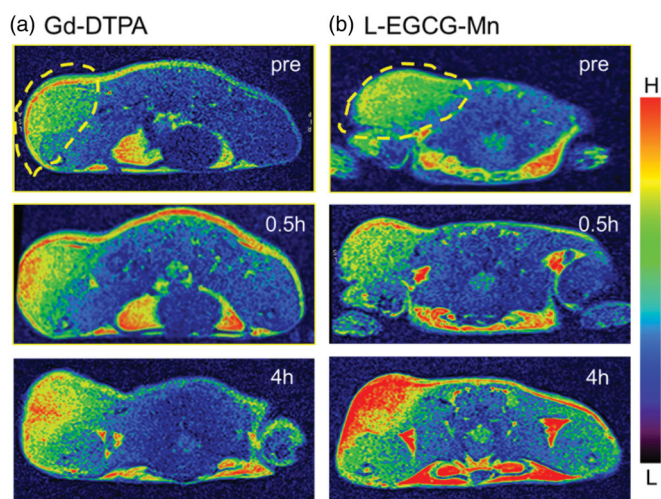


Figure 9. *In vivo* T1WI MR images (3 T) of H22 tumor-bearing mice pre- and post-intravenous injection (i.v.) with Gd-DTPA (a) or L-EGCG-Mn NPs (b). The images are displayed at a window width of 2588 and window level of 1324. L-EGCG-Mn NPs led to a higher enhancement of tumor contrast than Gd-DTPA.

provide a remarkable image-acquisition time window. This is mainly attributable to the enhanced permeability and retention effects (Kim et al., 2018) of NPs. Consequently, we can conclude that high tumor retention and rapid organ clearance makes L-EGCG-Mn NPs an efficient and safe CA.

The r_1 values of L-EGCG-Mn NPs in a buffer solution at 3 T MRI (pH 6.8, $4.18 \text{ mM}^{-1} \cdot \text{s}^{-1}$ and pH 5.5, $6.43 \text{ mM}^{-1} \cdot \text{s}^{-1}$) obtained in this study are comparable to those displayed by HMPB-Mn (Cai et al., 2015) in an aqueous solution at 7 T (pH 5, $7.43 \text{ mM}^{-1} \cdot \text{s}^{-1}$), PEGMnCaP (Mi et al., 2016) in buffer solution at 0.59 T (pH 6.7, $4.27 \text{ mM}^{-1} \cdot \text{s}^{-1}$), and by (UCNP@PFNS/N)@MnCaP (Ji et al., 2019) in an aqueous solution at 7 T (pH 6.8, $4.4 \text{ mM}^{-1} \cdot \text{s}^{-1}$ and pH 5, $6.9 \text{ mM}^{-1} \cdot \text{s}^{-1}$). However, the r_1 value of L-EGCG-Mn NPs in HSA (pH 6.8, $5.55 \text{ mM}^{-1} \cdot \text{s}^{-1}$) is lower than that of PEGMnCaP in HSA (pH 6.7, $15.26 \text{ mM}^{-1} \cdot \text{s}^{-1}$). A possible explanation is that the specific binding between EGCG and HSA limits the binding of Mn^{2+} and HSA (Save & Choudhary, 2018). Interestingly, pH-sensitive CAs, namely L-EGCG-Mn, USMO@MSNs (Wang et al., 2018), and MnO_2 nanosheets (Chen et al., 2014), are all designed to make the NP core be the most exposed to water molecules in an acidic environment, thereby improving the

accessibility of water molecules and Mn^{2+} . However, the r_1 value found in this study is higher than that determined for USMO@MSNs ($5.61 \text{ mM}^{-1} \cdot \text{s}^{-1}$ in buffer solution, pH 4.5 at 9.4 T MR) and delaminated MnO_2 nanosheets ($4.0 \text{ mM}^{-1} \cdot \text{s}^{-1}$ in buffer solution, pH 4.6 at 3 T MR). This may be due to the fact that the acidic environment can weaken the chelation of EGCG and Mn, thereby substantially accelerating the release of Mn^{2+} . Furthermore, the difference in relaxivity may also be associated with the different experimental conditions used, as there are many factors that can influence relaxivity, including solvent type, incubation time, and even temperature (Hao et al., 2012; Goetschi et al., 2014). L-EGCG-Mn NPs also showed pH sensitivity in terms of shortening the T_2 relaxation time, which is similar to previous studies (Chen et al., 2012).

The high relaxivity of L-EGCG-Mn NPs encouraged us to further explore its MRI performance *in vivo*. We found that the *in vivo* MRI performance of L-EGCG-Mn NPs was comparable to that of the pH-responsive HMPB-Mn (Cai et al., 2015), PEGMnCaP (Mi et al., 2016), and (UCNP@PFNS/N)@MnCaP (Ji et al., 2019). However, the peak SI of HMPB-Mn appeared at approximately 30 min, whereas that of L-EGCG-MN NPs appeared at 1 h. This may be due to the fact that the HMPB-Mn NPs were administrated via intratumor injection. Additionally, L-EGCG-Mn NPs mainly exhibited a homogeneous enhancement, which is different from the selective high strengthening of PEGMnCaP and (UCNP@PFNS/N)@MnCaP. The significantly lower concentration of Mn used in this study ($6.4 \mu\text{mol/kg}$) may be a potential explanation, as well as the use of a different tumor type (H22 tumors) when compared to existing studies (PEGMnCaP: $225 \mu\text{mol/kg}$ based on Mn for C26 tumors; UCNP@PFNS/N @MnCaP: $750 \mu\text{mol/kg}$ based on Mn for HepG2 tumors).

The above-mentioned Mn-based CAs are still in the basic research stage. Therefore, although they are useful as a reference for comparison against L-EGCG-Mn NPs, it is also important to compare L-EGCG-Mn NPs with clinically used CAs. Thus, the first approved extracellular Gd chelate, namely Gd-DTPA, was used to compare the properties of L-EGCG-Mn NPs. *In vitro* experiments showed that the T_1 and T_2 relaxivity of L-EGCG-Mn NPs were significantly higher than those of Gd-DTPA. Moreover, in the H22 tumor-bearing mice model, L-EGCG-Mn NPs led to improved SNR and CNR when

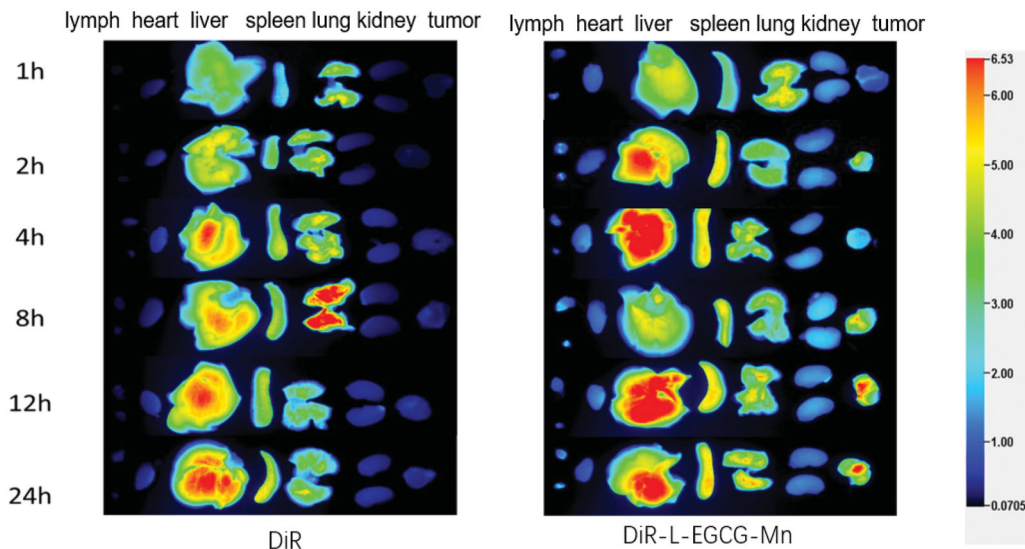


Figure 10. Fluorescence imaging and *ex vivo* distribution of L-EGCG-Mn NPs. *Ex vivo* image of the inguinal lymph nodes, heart, liver, spleen, lungs, kidneys, and tumor of H22 tumor-bearing KM mice injected with DiR and DiR-L-EGCG-Mn NPs for 1, 2, 4, 8, 12, and 24 h.

compared to Gd-DTPA in T1WI. In addition to the pH sensitivity of L-EGCG-Mn NPs, it is also possible that this may be due to the fact that Gd-DTPA has only one water molecule coordination site due to the DTPA ligand forming a stable structure around Gd^{3+} (Cai et al., 2015).

Additionally, histochemical analysis showed that the inguinal lymph nodes exhibited inflammatory hyperplasia, possibly as an effect of the neoplasm. Interestingly, analysis of *in vivo* distribution showed that the aggregation of L-EGCG-Mn NPs in the lymph nodes increased with time. This phenomenon may be explained by the acidic microenvironment created due to inflammatory hyperplasia (Gallagher et al., 2008). Thus, the relationship between inflammatory tissues and Mn NPs needs further study.

Conclusions

This study developed EGCG-Mn NPs enveloped with phospholipids and thus obtained NPs with a good safety profile and high pH sensitivity that may be used as MRI CAs. L-EGCG-Mn NPs could respond to tumor-related pH changes and, therefore, may serve as a potential tumor-targeting CA due to its good MRI properties in both a hypoxic cell model and H22 tumor-bearing mice model.

Acknowledgements

The authors thank the Analytical and Testing Center of Huazhong University of Science and Technology for TEM analysis.

Disclosure statement

The author reports no conflicts of interest in this work.

Funding

This work was supported by the National Natural Science Foundation of China under Grant numbers: 82071890, 81701657, 81673374, 81872810, 81571642, and 81771801, the Fundamental Research Funds for the Central Universities under Grant numbers: 2018KFYXJJ019 and 2019KFYRCPY049, Wuhan Science and Technology Plan for Applied Fundamental Research under Grant number 2017060201010146.

References

- Adisheshaiah P, Dellinger A, MacFarland D, et al. (2013). A novel gadolinium-based trimetaspere metallofullerene for application as a magnetic resonance imaging contrast agent. *Invest Radiol* 48:745–54.
- Bao Y, Yin M, Hu X, et al. (2016). A safe, simple and efficient doxorubicin prodrug hybrid micelle for overcoming tumor multidrug resistance and targeting delivery. *J Control Release* 235:182–94.
- Cai X, Gao W, Ma M, et al. (2015). A Prussian Blue-based core-shell hollow-structured mesoporous nanoparticle as a smart theranostic agent with ultrahigh pH-responsive longitudinal relaxivity. *Adv Mater* 27: 6382–9.
- Calcagno V, Vecchione R, Quagliariello V, et al. (2019). Oil core-PEG shell nanocarriers for *in vivo* MRI imaging. *Adv Healthc Mater* 8:e1801313.
- Chang CH, Qiu J, O'Sullivan D, et al. (2015). Metabolic competition in the tumor microenvironment is a driver of cancer progression. *Cell* 162: 1229–41.
- Chen Y, Ye D, Wu M, et al. (2014). Break-up of two-dimensional MnO_2 nanosheets promotes ultrasensitive pH-triggered theranostics of cancer. *Adv Mater* 26:7019–26.
- Chen Y, Yin Q, Ji X, et al. (2012). Manganese oxide-based multifunctionalized mesoporous silica nanoparticles for pH-responsive MRI, ultrasonography and circumvention of MDR in cancer cells. *Biomaterials* 33:7126–37.
- Dekkers IA, Roos R, van der Molen AJ. (2018). Gadolinium retention after administration of contrast agents based on linear chelators and the recommendations of the European Medicines Agency. *Eur Radiol* 28: 1579–84.
- Dubbelboer IR, Pavlovic N, Heindryckx F, et al. (2019). Liver cancer cell lines treated with doxorubicin under normoxia and hypoxia: cell viability and oncologic protein profile. *Cancers* 11:1024.

- Erstad DJ, Ramsay IA, Jordan VC, et al. (2019). Tumor contrast enhancement and whole-body elimination of the manganese-based magnetic resonance imaging contrast agent Mn-PyC3A. *Investig Radiol* 54: 697–703.
- Fries P, Muller A, Seidel R, et al. (2015). P03277—a new approach to achieve high-contrast enhancement: initial results of an experimental extracellular gadolinium-based magnetic resonance contrast agent. *Investig Radiol* 50:835–42.
- Fu C, Duan X, Cao M, et al. (2019). Targeted magnetic resonance imaging and modulation of hypoxia with multifunctional hyaluronic acid-MnO₂ nanoparticles in glioma. *Adv Healthcare Mater* 8:e1900047.
- Gale EM, Atanasova IP, Blasi F, et al. (2015). A manganese alternative to gadolinium for MRI contrast. *J Am Chem Soc* 137:15548–57.
- Gale EM, Wey HY, Ramsay I, et al. (2018). A manganese-based alternative to gadolinium: contrast-enhanced MR angiography, excretion, pharmacokinetics, and metabolism. *Radiology* 286:865–72.
- Gallagher FA, Kettunen MI, Day SE, et al. (2008). Magnetic resonance imaging of pH in vivo using hyperpolarized ¹³C-labelled bicarbonate. *Nature* 453:940–3.
- Garcia-Hevia L, Banobre-Lopez M, Gallo J. (2019). Recent progress on manganese-based nanostructures as responsive MRI contrast agents. *Chemistry* 25:431–41.
- Goetschi S, Froehlich JM, Chuck NC, et al. (2014). The protein and contrast agent-specific influence of pathological plasma-protein concentration levels on contrast-enhanced magnetic resonance imaging. *Invest Radiol* 49:608–19.
- Grobner T. (2006). Gadolinium—a specific trigger for the development of nephrogenic fibrosing dermopathy and nephrogenic systemic fibrosis? *Nephrol Dial Transplant* 21:1104–8.
- Hao DP, Ai T, Goerner F, et al. (2012). MRI contrast agents: basic chemistry and safety. *J Magn Reson Imaging* 36:1060–71.
- Huang CC, Khu NH, Yeh CS. (2010a). The characteristics of sub 10 nm manganese oxide T1 contrast agents of different nanostructured morphologies. *Biomaterials* 31:4073–8.
- Huang J, Xie J, Chen K, et al. (2010b). HSA coated MnO nanoparticles with prominent MRI contrast for tumor imaging. *Chem Commun (Camb)* 46:6684–6.
- Ippolito L, Morandi A, Giannoni E, Chiarugi P. (2019). Lactate: a metabolic driver in the tumour landscape. *Trends Biochem Sci* 44:153–66.
- Ji Y, Lu F, Hu W, et al. (2019). Tandem activated photodynamic and chemotherapy: using pH-sensitive nanosystems to realize different tumour distributions of photosensitizer/prodrug for amplified combination therapy. *Biomaterials* 219:119393
- Jiang X, Sun Y, Shang L, et al. (2019). Green tea extract-assembled nano-clusters for combinational photothermal and chemotherapy. *J Mater Chem B* 7:5972–82.
- Kanamala M, Wilson WR, Yang M, et al. (2016). Mechanisms and biomaterials in pH-responsive tumour targeted drug delivery: a review. *Biomaterials* 85:152–67.
- Kim HJ, Yi Y, Kim A, Miyata K. (2018). Small delivery vehicles of siRNA for enhanced cancer targeting. *Biomacromolecules* 19:2377–90.
- Kim SM, Im GH, Lee DG, et al. (2013). Mn(2+)-doped silica nanoparticles for hepatocyte-targeted detection of liver cancer in T1-weighted MRI. *Biomaterials* 34:8941–8.
- Li B, Gu Z, Kurniawan N, et al. (2017). Manganese-based layered double hydroxide nanoparticles as a T1-MRI contrast agent with ultrasensitive pH response and high relaxivity. *Adv Mater* 29:1700373.
- Li J, Chen YC, Tseng YC, et al. (2010). Biodegradable calcium phosphate nanoparticle with lipid coating for systemic siRNA delivery. *J Control Release* 142:416–21.
- Li K, Xiao G, Richardson JJ, et al. (2019). Targeted therapy against metastatic melanoma based on self-assembled metal-phenolic nanocomplexes comprised of green tea catechin. *Adv Sci (Weinh)* 6:1801688.
- Luo M, Liu Z, Zhang X, et al. (2019). Synergistic STING activation by PC7A nanovaccine and ionizing radiation improves cancer immunotherapy. *J Control Release* 300:154–60.
- Marckmann P, Skov L, Rossen K, et al. (2006). Nephrogenic systemic fibrosis: suspected causative role of gadodiamide used for contrast-enhanced magnetic resonance imaging. *J Am Soc Nephrol* 17: 2359–62.
- Mi P, Kokuryo D, Cabral H, et al. (2016). A pH-activatable nanoparticle with signal-amplification capabilities for non-invasive imaging of tumour malignancy. *Nat Nanotechnol* 11:724–30.
- Navarro RE, Santacruz H, Inoue M. (2005). Complexation of epigallocatechin gallate (a green tea extract, EGCG) with Mn²⁺: nuclear spin relaxation by the paramagnetic ion. *J Inorg Biochem* 99:584–8.
- Neri D, Supuran CT. (2011). Interfering with pH regulation in tumours as a therapeutic strategy. *Nat Rev Drug Discov* 10:767–77.
- Ogg RJ, Kingsley PB. (2004). Optimized precision of inversion-recovery T1 measurements for constrained scan time. *Magn Reson Med* 51:625–30.
- Pan D, Schmieder AH, Wickline SA, Lanza GM. (2011). Manganese-based MRI contrast agents: past, present and future. *Tetrahedron* 67:8431–44.
- Peng W, Huang W, Ge X, et al. (2019). Type I gamma phosphatidylinositol phosphate kinase promotes tumor growth by facilitating Warburg effect in colorectal cancer. *EBioMedicine* 44:375–86.
- Peng Y, Li Z, Tang H, et al. (2018). Comparison of reduced field-of-view diffusion-weighted imaging (DWI) and conventional DWI techniques in the assessment of rectal carcinoma at 3.0T: image quality and histological T staging. *J Magn Reson Imaging* 47:967–75.
- Pilon-Thomas S, Kodumudi KN, El-Kenawi AE, et al. (2016). Neutralization of tumor acidity improves antitumor responses to immunotherapy. *Cancer Res* 76:1381–90.
- Pintaske J, Martirosian P, Graf H, et al. (2006). Relaxivity of gadopentetate dimeglumine (Magnevist), gadobutrol (Gadovist), and gadobenate dimeglumine (MultiHance) in human blood plasma at 0.2, 1.5, and 3 Tesla. *Invest Radiol* 41:213–21.
- Rahim MA, Bjornmalm M, Bertleff-Zieschang N, et al. (2018). Multiligand metal-phenolic assembly from green tea infusions. *ACS Appl Mater Interfaces* 10:7632–9.
- Reddi AR, Jensen LT, Culotta VC. (2009). Manganese homeostasis in *Saccharomyces cerevisiae*. *Chem Rev* 109:4722–32.
- Reygaert WC. (2014). The antimicrobial possibilities of green tea. *Front Microbiol* 5:434.
- Reygaert WC. (2018). Green tea catechins: their use in treating and preventing infectious diseases. *Biomed Res Int* 2018:9105261.
- Save SN, Choudhary S. (2018). Elucidation of energetics and mode of recognition of green tea polyphenols by human serum albumin. *J Mol Liq* 265:807–17.
- Shen Y, Goerner FL, Heverhagen JT, et al. (2019). In vitro T2 relaxivities of the Gd-based contrast agents (GBCAs) in human blood at 1.5 and 3 T. *Acta Radiol* 60:694–701.
- Shen Y, Goerner FL, Snyder C, et al. (2015). T1 relaxivities of gadolinium-based magnetic resonance contrast agents in human whole blood at 1.5, 3, and 7 T. *Investig Radiol* 50:330–8.
- Shin J, Anisur RM, Ko MK, Im GH, et al. (2009). Hollow manganese oxide nanoparticles as multifunctional agents for magnetic resonance imaging and drug delivery. *Angew Chem Int Ed Engl* 48:321–4.
- Swartz MA, Iida N, Roberts EW, et al. (2012). Tumor microenvironment complexity: emerging roles in cancer therapy. *Cancer Res* 72:2473–80.
- Tsai LC, Hsieh HY, Lu KY, et al. (2016). EGCG/gelatin-doxorubicin gold nanoparticles enhance therapeutic efficacy of doxorubicin for prostate cancer treatment. *Nanomedicine (Lond)* 11:9–30.
- Wang C, Sang H, Wang Y, et al. (2018). Foe to friend: supramolecular nanomedicines consisting of natural polyphenols and bortezomib. *Nano Lett* 18:7045–51.
- Wang D, Lin H, Zhang G, et al. (2018). Effective pH-activated theranostic platform for synchronous magnetic resonance imaging diagnosis and chemotherapy. *ACS Appl Mater Interfaces* 10:31114–23.
- Xiao L, Mertens M, Wortmann L, et al. (2015). Enhanced in vitro and in vivo cellular imaging with green tea coated water-soluble iron oxide nanocrystals. *ACS Appl Mater Interfaces* 7:6530–40.
- Zhang W, Wang G, Xu ZG, et al. (2019). Lactate is a natural suppressor of RLR signaling by targeting MAVS. *Cell* 178:176–189.e15.
- Zheng S, Zhang M, Bai H, et al. (2019). Preparation of AS1411 aptamer modified Mn-MoS₂ QDs for targeted MR imaging and fluorescence labelling of renal cell carcinoma. *Int J Nanomedicine* 14:9513–24.
- Zhuang X, Wu T, Zhao Y, et al. (2016). Lipid-enveloped zinc phosphate hybrid nanoparticles for codelivery of H-2K(b) and H-2D(b)-restricted antigenic peptides and monophosphoryl lipid A to induce antitumor immunity against melanoma. *J Control Release* 228:26–37.